Cloud Resolving Model Applied to Nowcasting: An evaluation of Data Assimilation and Microphysics Parameterization

Eder P. Vendrasco[1*], Luiz A. T. Machado[1], Bruno Z. Ribeiro[1] and Edmilson D. Freitas[2]

[1]Center for Weather Forecast and Climate Studies, National Institute for Space Research (CPTEC/INPE), Cachoeira Paulista, SP, Brazil.
[2]Institute of Astronomy, Geophysics and Atmospheric Sciences, University of Sao Paulo (IAG/USP), Sao Paulo, SP, Brazil.

[*]Correspondence to: Eder P. Vendrasco, Center for Weather Forecast and Climate Studies, National Institute for Space Research (CPTEC/INPE), Rodovia Presidente Dutra, km 39, Cachoeira Paulista - SP, Brasil, 12630-000. E-mail: eder.vendrasco@inpe.br

ABSTRACT:

Keywords: radar data assimilation; WRF; SOS-CHUVA; southeastern Brazil; severe thunderstorm.

1. Introduction

Accurate short-term high-resolution precipitation forecast has been a challenge since the last few decades. The computing power has increased allowing the increasing in model grid resolution, however, the accuracy in predicting the time and position of a particular convective cell is still reduced, especially in the first forecast hours. One of the reasons that causes this low skill at the very beginning of the forecast is the well-known spin-up problem (Illari, 1987). It becomes more relevant when doing short-term weather forecast (1-6h). For precipitation prediction up to 3 hours, Lagrangian advection of radar echoes usually performs better compared to numerical weather prediction (Lin et al., 2005; Sun et al., 2014). Of course, it depends on the rain system type, i.e., less organized convection has a forecast range much shorter than those well-organized (Zipser, 1990). In the range between around 3 to 6 hours there is a gap in performance between extrapolation methods and dynamical numerical models. In order to fill this gap, many studies have been done to reduce the spin-up of numerical models (Sun et al., 2014), and the best way to improve the model skill at the very beginning of the precipitation forecast is to better represent the model initial condition (Stensrud et al., 2013), and it can be accomplished by performing data assimilation (Sun et al., 2014). Data assimilation (DA) is a technique for generating accurate image of the true state of the atmosphere at a given time in which the observed information is accumulated into the model state by taking advantage of consistency constraints with laws of time evolution and physics properties. A crucial advantage of NWP models with Data Assimilation (DA) compared to nowcasting models (extrapolation of radar echoes) is that it not only adds the current data into the NWP model, but they should also initialize convective-scale events (Sokol, 2010). A logical approach used for nowcasting is to blend radar echo extrapolation with a numerical model to generate a seamless 0-6h forecast (Sun et al., 2014). However, extrapolation skill is strongly reduced with time and the blended forecast after 3-4h will rely on the numerical models.

Initial condition plays a crucial role in numerical weather prediction (NWP) and for high resolution forecasts the model needs to be initialized not only using observation that describe the large-scale features, but also the convective scale. Understanding how to assimilate observations at the convective scale, resolving the dynamical process relevant for predicting convection and dealing with rapid error growth is a huge challenge. Doppler Radar observations have been used in complex DA systems in order to improve the initial condition of high-resolution models, since they are almost the only source of three-dimensional data in this scale (Aksoy et al., 2009). Reflectivity and radial velocities from doppler radars have been successfully used in complex DA in order to improve the initial condition for convection-permitting models (e.g., Gao et al., 2004; Sun et al., 2005; Xiao et al., 2007; Ming at al., 2009; Wang et al., 2013; Vendrasco et al., 2016; Tong et al., 2016; Kong et al., 2018). More recently, polarimetric variables have also been used in DA systems (eg., Carlin et al., 2017; Li et al., 2017; Kawabata et al., 2018; Wolfensberger and Berne, 2018). Although, many studies have shown improvements on the precipitations forecasts due to radar DA, it still a challenge to extract as much information as possible from observations while maintaining the large-scale balance found in the background. Vendrasco et al. (2016) have shown that constraining the cost function with a large-scale analysis can alleviate this problem. Also, Tong et al. (2016) have studied the best cycle strategy to assimilate radar data and they found that performing 3 1-h cycle before the analysis time gave them the best results compared to 3-h cycle.

Another important aspect that directly impacts the precipitation in high resolution forecasts is the microphysical parameterization. Many approaches are considered to parametrize the in-cloud process and they can be categorized in two schemes: bulk and bin parameterizations. Bin schemes aims to calculate microphysics as accurately and generally as possible. It divides microphysical particles in bins for different sizes and compute the evolution of each bin separately. Thus, the particle size distribution (PSD) is an output, instead of an input like occurs in bulk schemes. Although it is much more general and precise, it is very expensive computationally and it is not feasibly in operational NWP models. Bulk schemes can be classified by the number of moments (predicted variables) that is included in the parametrization. The most common bulk parameterizations are those with single moments (e.g, Ferrier – Ferrier et al. 2002; WSM6 - Hong and Lim 2006; Thompson - Thompson et al. 2008) that predict only the mass of the particles, and the double moment bulk schemes that predict also the number of concentration (e.g., WDM6 – Lim and Hong 2010; Morrinson – Morrinson et al. 2009). It is not common in operational NWP models, but there are also developments in bulk schemes with the third moment, which provides the prediction of reflectivity as well (e.g., Milbrandt and Yau, 2005). Many works have shown the impact of microphysical parameterization on high resolution precipitation forecast (Wu et al, 2013), however, just a few have discussed their impact while doing radar DA. Although all the bulk microphysics parameterizations solve similar process, the production of rain and its timing can also be distinct. The question that raises is: does the radar DA produce any impact on this behavior?

The goal of this paper is to evaluate the performance of cloud resolving model for nowcasting application of intense thunderstorms and provides some evaluations regarding the impact of different radar DA procedures and microphysics parameterization.

This paper is organized as follows: Section 2 presents the SOS-CHUVA project, the radar data used in this work and outlines the experimental setup. Also, it briefly describes the WRF 3DVAR DA system employed in this study and the methods for precipitation verification. In Section 3 is presented the evaluation of DA procedure (i.e., the increments and residuals) and the short-range precipitation forecast for 5 convective cases to show how the radar DA and the different microphysics impacts the precipitation forecast in the first 6 hours of leading time. The main results obtained from this study are summed up in Section 4.

2. Data and Methodology

2.1. The SOS-CHUVA campaign

The SOS-CHUVA campaign occurred in south-eastern Brazil between 2016 and 2018. The campaign was a collaborative effort of several Brazilian institutions to better understand severe thunderstorms in the region and improve nowcasting tools and methodologies. SOS-CHUVA is an extension of the CHUVA project (Machado et al., 2014) specially dedicated to nowcasting. During the experiment, several instruments were installed and operated during two years (2016-2018) in Campinas, São Paulo State (Fig. 1), in special an X-band polarimetric radar and two others operational S band radars.

FIGURA 1

2.2. Selection of the cases

Five cases of intense/severe storms were selected among all the cases occurred during the SOS-CHUVA campaign (Fig. 2). The 5 cases were chosen based on their intensity and the availability of data, particularly the radar data. Also, there was an attempt to include cases of convective systems with different morphologies, from organized mesoscale convective systems, such as quali-linear convective systems (QLCS) and storm clusters, to isolated storms. For all cases, severe/intense weather was reported, including hail, strong winds and/or flooding, see Fig. 2. A synthesis of these cases, as well as the radar data used in the data assimilation system, is shown in Table 1. A more detailed discussion of the events and the synoptic-scale environment is shown in Sec. 3.1.

FIGURA 2

2.3. Radars data

The three radars employed in this study were located in: São Roque (23.602°S, 47.094°W, 1147 m altitude; ***SR***), Salesópolis (23.600°S, 45.972°W, 916 m altitude; ***SL***) and Campinas (22.813°S, 47.056°W, 680 m altitude; ***CP***), see Fig. 1 and Table 2 for a detailed description of all radars. The volumetric data is available each 5 minutes for the ***CP*** radar and 10 and 15 minutes for the ***SR*** and ***SL*** radars, respectively. In this study, only volumetric data every 60 minutes were used in the DA cycling process. Data every 30 minutes were used for the forecast evaluation.

2.4. WRF and WRFDA

The model used in the study was the Weather Research and Forecasting model (WRF-ARW - Skamarock, 2008), version 3.9.1.1, and its 3DVAR data assimilation system (WRFDA-3DVAR), version 3.9.1 (Baker et al., 2004). It iteratively minimizes the cost function defined by:

$$J = J_b + J_o = \frac{1}{2}\mathbf{v}^T\mathbf{v} + \frac{1}{2}(\mathbf{d} - \mathbf{H}'\mathbf{U}\mathbf{v})^T\mathbf{R}^{-1}(\mathbf{d} - \mathbf{H}'\mathbf{U}\mathbf{v}) \quad (1)$$

where J_b and J_o stand for the background (i.e., the previous model forecast) and observation terms, respectively. The term $\mathbf{v}$ is the control variable (CV) defined by $\mathbf{v} = \mathbf{U}^{-1}(\mathbf{x} - \mathbf{x}_b)$, where $\mathbf{U}$ is the decomposition of the background error covariance $\mathbf{B}$ via $\mathbf{B} = \mathbf{U}\mathbf{U}^\mathbf{T}$; $\mathbf{x}$ is the full analysis variable; and $\mathbf{x}_b$ is the background variable. The innovation vectors that measures the departure of the observation $\mathbf{y}_0$ from its counterpart computed from the background $\mathbf{x}_b$ is given by $\mathbf{d} = \mathbf{y}_0 - \mathbf{H}(\mathbf{x}_b)$. Here, $\mathbf{H}'$ is the linearization of the nonlinear observation operator $\mathbf{H}$, and $\mathbf{R}$ is the observation error covariance matrix.

Following Sun et al. (2016), the CV used in this study are velocity components u and v, temperature T, surface pressure Ps, and pseudo-relative humidity (RHs, where the humidity is divided by its background). For reflectivity data assimilation, the retrieved rainwater mixing ratio was used as CV, following Wang et al. (2013), in order to avoid the nonlinearities issues caused by the linearization of the observation operator, required by the incremental formulation (Courtier et al., 1994).

2.5. Model configuration

The Global Forecast System (GFS) forecasts, from the National Centers for Environmental Prediction (NCEP) were used as initial and boundary conditions (IC/BC) for the outermost WRF domain (d01). The GFS is a T1534 global model with 64 vertical levels. The model output is interpolated to a 0.25° resolution grid, which is used in this study. Both the IC/BC and the synoptic scale analysis of each case used the 1200 UTC GFS runs.

Four microphysics schemes were employed: Thompson, Morrison, WDM6 (WRF Double-Moment 6-Class) and WSM6 (WRF Single-Moment 6-Class). The four microphysics schemes combined with four DA methodologies, including no DA, resulted in sixteen runs for each case. See Table 3 for the description of the different running configuration. These runs were used to verify which one is the best combination of microphysics scheme and assimilation methodology, and also to evaluate the sensitivity of each factor separately (Sec. 3.2).

The cycling methodology is described in Fig. 3. For all 5 cases four continuously cycled analyses were performed at 1500, 1600, 1700 and 1800 UTC and then a 6-h forecast ensued. For the experiments labelled as nCYnDA and nCYyDA the cycling was not performed, instead the one-time DA at 1800 UTC was run and then a 6-h forecast took place.

FIGURE 3

2.6. Statistical verification

Several statistical indices were calculated using the composite reflectivity field generated by the simulations and the composite reflectivity field observed by the radars. The contingency table (Table 3) is used to evaluate the simulation reflectivity field in respect to its observed counterpart. The total numbers of hits, misses, false alarms and correct negatives in the domain are used to calculate the false alarm ratio (FAR; Eq. 1), the probability of detection (POD; Eq. 2) and the critical success index (CSI; Eq. 3).

$$FAR = \frac{falsealarms}{falsealarms + hits} \tag{1}$$

$$POD = \frac{hits}{hits + misses} \tag{2}$$

$$CSI = \frac{hits}{hits + misses + falsealarms} \tag{3}$$

The other indices used to evaluate the simulations are the root-mean square error (RMSE; Eq. 4) and the fractional skill score (FSS; Eq. 5; Roberts and Lean, 2008). The FSS is calculated using the reflectivity thresholds of 30, 40 and 50 dBZ and radii of 1, 2 and 3 km.

$$RMSE = \sqrt{\frac{1}{N}\sum_{k=1}^{N}(\bar{F}_k - \bar{O}_k)^2} \tag{4}$$

where F and O stands for the forecast and observed reflectivity field, respectively, the k subscript represents the k_{th} grid point and N the total number of grid points.

$$FSS = 1 - \frac{FBS}{FBS_w}$$
$$= 1 - \frac{\frac{1}{N}\sum_{k=1}^{N}\left(P_{F(k)} - P_{O(k)}\right)}{\frac{1}{N}\left[\sum_{k=1}^{N}\left(P^2{}_{F(k)} + P^2{}_{O(k)}\right)\right]} \qquad (5)$$

where the $P_{F(k)}$ and $P_{O(k)}$ are the fractional coverages of reflectivity in the k_{th} grid point that exceeds a given threshold and N is the total number if grid points in the domain.

3. Results

3.1. Cases description and synoptic environment

Figure 2 shows the composite radar reflectivity of the 5 cases used in this study. The time shown in Fig. 2 are approximately when severe weather was reported at surface, as indicated in the figure. The cases vary from mature quasi-linear convective systems (QLCS) (Figs. 2a,d) to isolated thunderstorms storms (Fig. 2b). This is an important characteristic of the cases selected because the results of this research are valid for intense events with different types of convective organization. The December 3rd case (Fig. 2a) is characterized by a large number of storms over the domain 3, including a QLCS in the northern part of the area that was attributed to several reports of severe winds in Campinas region. Isolated storms formed over the São Paulo metropolitan region in the afternoon of February 22nd (Fig. 2b) and caused hail and flash flooding in the area. On March 6th (Fig. 2c), a large area of precipitation covered most of the study region, with embedded severe storms in the northern sector causing hail and winds. The second QLCS among the studied cases occurred on May 5th (Fig. 2d), and was responsible for multiple severe wind reports and flooding. Finally, the October 27th (Fig. 2e) severe storms formed north of Campinas, presented Doppler velocity couplets indicating rotation during several radar scans (not shown), and were responsible for strong winds and hail.

The synoptic-scale 500-hPa configuration (Vorticity and winds at 500 hPa) at 1800 UTC for each case is shown in Fig. 4. At 1800 UTC of December 3rd (Fig. 4a), a cyclonic vorticity maximum was located upstream of the study region and caused lifting due to cyclonic vorticity advection (not shown). This trough was associated with colder air at 500 hPa (temperatures below –6°C), which increased the instability with time. The relatively strong 500-hPa flow (15–20 m s^{-1}) contributed to high wind shear and convective organization (Fig. 2a). Weak midlevel flow predominated in the study region during the isolated storms on February 22nd (Fig. 4b). The absence of a source of synoptic-scale lifting suggests these storms formed due to radiative surface heating and the increasing of thermodynamic instability during the afternoon. The case of March 6th (Fig. 4c) also occurred under weak midlevel flow, which contributed to the slow storm movement and the occurrence of flooding. Similar to the December 3rd case, on May 5th (Fig. 4d) a synoptic-scale trough upstream of the study region caused ascent and midlevel cold advection, and also contributed to intensify the wind shear and organize the QLCS. The storms occurred on October 27th formed downstream of a midlevel vorticity maximum embedded in strong zonal flow (Fig. 4e).

3.2. Results of DA: Increments and OMB/OMA profiles

This section shows the impact of radar DA on the analysis (i.e., the output from the DA system). Thus, only experiments with DA are considered, i.e. nCYyDA and yCYyDA. The first question addressed is regarding to the DA behavior for each microphysics.

Figure 5 shows the averaged vertical profiles of observation, innovation (observation minus background) and residual (observation minus analysis) for radial velocity and rainwater, snow and graupel mixing ratios. The first important result is that the residual is always close to zero on the entire profile. It means that the DA is capable of vanishing almost all the innovation and, thus, bringing the background closer to the observation. Another interesting finding is that while almost no difference is observed among microphysics in the radial velocity profile, and just a small difference in the rainwater mixing ratio, the snow and graupel profiles have shown the greatest differences. Figure 5 shows clearly that after 4 cycles, the Thompson microphysics parameterization produces much more snow then the others, on the other hand, Morrison microphysics produces much more graupel than observation, followed by WSM6 e WDM6. Although Thompson also overestimates graupel, it is much closer to observations than the other microphysics. Regarding rainwater, except for WDM6, the profiles are similar, showing small overestimation below 3 km and underestimation above that level. WDM6 overestimates the entire profile. It’s important to point out that the microphysics observations come from the estimation using the relationships from Gao and Stensrud (2012) that is employed in the WRFDA.

From the DA point of view, the overestimation of snow and graupel by Thompson and

Morrison microphysics parameterizations, respectively, triggers a balance problem. The greatest is the innovation, the greatest should be the analysis imbalance caused by the 3DVAR DA. The results showed in Fig. 5 for the residual is quite good, however, it should be taken into account that the average considers only where radar data are available, which means that where radars are not available the residuals keep large and it will affect the forecast started from that analysis. Also, because of this heterogeneous reduction of the residuals, the balance of the analysis is affected.

Figure 6 shows an example for case of December 3rd, 2016, of the innovations, increments and residuals of snow and graupel for each microphysics. It clearly shows overestimation of graupel and snow for Morrison and Thompson microphysics, also shows that the residuals is very small, which implies that the DA process was able to reduce the innovation. Figure 6 also shows large area without radar data, where DA could not correct the mentioned overestimation. Therefore, although the ability of DA to correct the microphysics concentrations clearly does not depend on the microphysics, the importance of choosing a proper parametrization is still an important step to get an accurate forecast.

3.3. Sensitivity to microphysics parameterization

In this section, the four microphysics schemes are evaluated for the five cases.

Figure 7 shows the RMSE and FSS (for the 30-dBZ threshold) of the average among all the five cases and all the four DA methods for each microphysics parameterization employed. The RMSE (Fig. 7a) in general decreases from 30 to 90 minutes of forecast, and then increases again. Simulations using the Thompson microphysics present the lowest RMSE in all forecast times, followed by the simulations using the Morrison scheme. The FSS (Fig. 7b), on the other hand, is lower in Thompson simulations, but the difference is small between all the microphysics schemes. In terms of the reflectivity pattern, simulations with Thompson have a better depiction of the convective and stratiform areas, while the other microphysics tend to overestimate the reflectivity values, as it will be shown latter. For this reason, in this study we will use the Thompson microphysics as a reference in the analysis of the different DA methods.

3.4.Sensitivity to radar DA method

This section presents the statistical verifications for the different DA methods. Firstly, two cases with relatively good and regular model performance are described. The model errors in representing convective and stratiform areas and how can the radar DA improve this can be accessed through the analysis of the reflectivity fields.

Figure 8 shows the observed and simulated composite reflectivity for the March 3rd case. The yCYyDA 1-h forecast (Fig. 8d) was able to reproduce the most intense storm in the area over the northwestern part of the domain (Fig. 8a), even though the location is shifted to North, compared to observation. In the southern part of the domain (around the 24°S latitude), the west-east band of precipitation observed at 2100 UTC (Fig. 8c) is formed in the simulation 2 h earlier (Fig. 8d), and by 2100 UTC (Fig. 8f) it has dissipated in the model. By comparing the yCYyAD simulation (Fig. 8d,e,f) with the nCYyAD simulation (Fig. 8g,h,i), the DA cycle causes a better representation of the severe thunderstorms in the northwestern part of the domain with 1 hour of forecast. The precipitation band that remains after the severe storms dissipate at 2000 and 2100 UTC

(2- and 3-h forecasts, respectively) is broader in the yCYyDA simulation (Fig. 8d,e,f), which better agrees with the observation. Other noteworthy characteristic is the larger area with precipitation over the domain in the yCYyDA simulation when compared to all the other simulations (Fig. 8g–o), which is observed in all simulated cases (not shown).

The simulations without radar DA (yCYnDA and nCYnDA) show a lower precipitation coverage over the domain (Figs. 8j–o) when compared to the simulations with radar DA (Figs. 8d–i). The yCYnAD (Figs. 8j–l) simulation presents a better representation of the severe storms north of 19°S relative to the nCYnAD (Figs. 8m–o) simulation in all forecast hours, and is similar to the yCYyAD (Figs. 8d–f) simulation in this aspect. The model run with a previous precipitation in the model, which is generated by the cycle, does a better job in simulating the severe storms in the area. The simulation without DA and without cycle presents a much lower precipitation coverage than observed, mainly in the first hour of forecast (Fig. 8m). It is explained by the spin-up problem that take time to balance the model and initiate convection.

Figure 9 shows the radar reflectivity factor and 2-h simulated reflectivity forecasts valid for 2000 UTC 22 February 2017, when an isolated storm produced small hail and flooding in the city of São Paulo. Similar to what occurred to the other cases (Fig. 8a–f), the yCYyDA simulation (Fig. 9b) forecasts precipitation over a larger area compared to observation (Fig. 9a). The overestimated precipitation area is possibly related to the character of precipitation: as the radar indicates several storms over the region and the thermodynamic environment is considerably unstable (CAPE > 2000 J kg^{-1}, not shown), the cycle and DA causes convective overturn throughout the domain. It is also possible that non-meteorological radar echoes (e.g., areas with reflectivity factor lower than 20 dBZ between 23°S and 24°S, 47°W and 48°W) are being interpreted by the model as areas of active convection. Despite the widespread precipitation area in yCYyDA simulation, the area of severe convection over the São Paulo metropolitan area is relatively well indicated by the model.

The yCYnDA simulation (Fig. 9d) produces the best results in this case because it is able to forecast the severe thunderstorm very close to the observed storm (Fig. 9a) and does not produce precipitation over a wide area as the yCYyDA (Fig. 9b), which suggests the DA is the reason for the overestimated precipitation in yCYyDA simulation. Both simulations without cycle, nCYyDA (Fig. 9e) and nCYnDA (Fig. 9f), fail to forecast the severe storm with 2 hours of simulation and in future times (not shown). These results suggest that the cycle is important in place the storms correctly.

Given the inability of the yCYyAD simulation for the February 22nd case in forecasting the discrete convective mode that was observed, a test was performed in which the radius of influence of the observations (radar reflectivity field) is decreased. Fig. 9c shows the results of this simulation. There is no evident improvement in the forecasted reflectivity field for this case. The characteristic of the convection remains more widespread than observed (Fig. 9a).

The temporal evolution of the average statistical indices, for all five cases, is shown in Fig. 10. These indices are averages of the simulations of all cases and all microphysics schemes for each DA method. The RMSE (Fig. 10a) is lower in the yCYyAD simulations for the entire period, except in the 1-h forecast, when it is lower than the nCYyAD RMSE. Both simulations with radar DA have lower RMSE than simulations without radar DA. Also, the RMSE increases with time in the simulations with radar DA, but is less variable in simulations without radar DA. The CSI (Fig. 10b) shows similar results, with higher CSI in simulations that use radar DA. For most DA methods, the CSI increases with time, which is unexpected since the forecast skill tends to decrease with time. However, most of the cases had greater thunderstorms coverage in the area in the first hours of forecast (most severe weather reports occurred between 18 and 19 UTC), so the CSI tends to increase when the stratiform precipitation dominates the convective precipitation or the precipitation leaves the domain.

Both POD (Fig. 10c) and FAR (Fig. 10d) agree with the general characteristic of yCYyDA to overestimate the precipitation area. The POD is much higher in the yCYyDA simulations, and the lowest POD occurs in simulations without cycle and without DA (nCYnDA). The FAR, on the other hand, is very similar in all DA methods. The combination of these two indices is better (higher POD and lower FAR) in the yCYyDA, which evidence the ability of the radar DA to better localize the storms in the simulation according to what the radar is observing in the analysis time.

4. Conclusions

Acknowledgements. The authors thank the Foundation for Research Support of Sao Paulo (Fapesp Grant 2015/14497-0).

References

Altuğ Aksoy*, David C. Dowell, and Chris Snyder, 2009: A Multicase Comparative Assessment of the Ensemble Kalman Filter for Assimilation of Radar Observations. Part I: Storm-Scale Analyses. Monthly weather review, **137**, 1805-1824. https://doi.org/10.1175/2008MWR2691.1

Barker, D. M., W. Huang, Y.-R. Guo, A. J. Bourgeois, and Q. N. Xiao, 2004: A three-dimensional variational (3DVAR) data assimilation system for use with MM5: Implementation and initial results. Mon. Wea. Rev., 132, 897–914, doi:10.1175/ 1520-0493(2004)132,0897:ATVDAS.2.0.CO;2.

J.T. Carlin, J. Gao, J.C. Snyder, A.V. Ryzhkov. Assimilation of ZDR columns for improving the spinup and forecast of convective storms in storm-scale models: Proof-of-concept experiments. Mon. Weather Rev., 145 (2017), pp. 5033-5057, 10.1175/MWR-D-17-0103.1

Courtier, P., J. N. Thepaut, and A. Hollingsworth, 1994: A strategy for operational implementation of 4D-Var, using an in- cremental approach. Quart. J. Roy. Meteor. Soc., 120, 1367– 1387, doi:10.1002/qj.49712051912

Ferrier, B. S., Y. Jin, T. Black, E. Rogers, and G. DiMego, 2002: Implementation of a new grid-scale cloud and precipitation scheme in NCEP Eta model. Preprints, 15th Conf. on Nu- merical Weather Prediction, San Antonio, TX, Amer. Meteor. Soc., 280–283.

Gao, J., Xue, M., Brewster, k., Droegemeier, k. k.. A Three-Dimensional Variational Data Analysis Method with Recursive Filter for Doppler Radars. J. of

Atmos. and Ocean. Tech., 21, 457-469.

Gao, J., and D. J. Stensrud, 2012: Assimilation of reflectivity data in a convective-scale, cycled 3DVAR framework with hydrometeor classification. J. Atmos. Sci., 69, 1054–1065, doi:https://doi.org/10.1175/JAS-D-11-0162.1

Hong, S.–Y., and J.–O. J. Lim, 2006: The WRF single–moment 6–class microphysics scheme (WSM6). J. Korean Meteor. Soc., 42, 129–151.

Illari, L., 1985: The "spin-up" problem. ECMWF Tech. Memo., **137**.

Charles Lin, Slavko Vasić, Alamelu Kilambi, Barry Turner, Isztar Zawadzki, 2005. Precipitation forecast skill of numerical weather prediction models and radar nowcasts. Geophis. Res. Letters, **32**, L14801. https://doi.org/10.1029/2005GL023451.

Takuya Kawabata, Thomas Schwitalla, Ahoro Adachi, Hans-Stefan Bauer, Volker Wulfmeyer, Nobuhiro Nagumo, and Hiroshi Yamauchi. Observational operators for dual polarimetric radars in variational data assimilation systems (PolRad VAR v1.0). Geosci. Model Dev., 11, 2493–2501, 2018 https://doi.org/10.5194/gmd-11-2493-2018.

Kong R, Xue M, Liu C. 2018. Development of a hybrid En3DVar data assimilation system and comparisons with 3D-Var and EnKF for radar data assimilation with observing system simulation experiments. Monthly Weather Review 146: 175–198.

Li X, Mecikalski JR, Posselt D. 2017. An ice-phase microphysics forward model and preliminary results of polarimetric radar data assimilation. Monthly Weather Review: 683–708, https://doi.org/10.1175/mwr-d-16-0035.1.

Lim, K.–S. S., and S.–Y. Hong, 2010: Development of an effective double–moment cloud microphysics scheme with prognostic cloud condensation nuclei (CCN) for weather and climate models. Mon. Wea. Rev., 138, 1587–

1612.doi:10.1175/2009MWR2968.1.

Machado, L.A.T.; Silva Dias, M.A.F.; Morales, C.; Fisch, G.; Vila, D.; Albrecht, R.; Goodman, S.J.; Calheiros, A.J.P.; Biscaro, T.; Kummerow, C.; et al. The CHUVA Project. How Does Convection Vary across Brazil? Bull. Am. Meteorol. Soc. 2014, 95, 1365–1380

Ming, C., S. Y. Fan, J. Zhong, X. Y. Huang, Y. R. Guo, W. Wang, Y. Wang, and B. A. Kuo, 2009: A WRF-based rapid updating cycling forecast system of BMB and its performance during the summer and Olympic Games 2008. Symp. on Nowcasting and Very Short Term Forecasting, Whistler, BC, Canada, WMO. [Available online at http://www2.mmm.ucar.edu/wrf/ users/workshops/WS2010/presentations/session%203/3A-5_ MinChen.pdf.]

Milbrandt, J. A., and M. K. Yau, 2005: A multimoment bulk microphysics parameterization. Part II: A proposed three–moment closure and scheme description. J. Atmos. Sci., 62, 3065–3081.

Morrison, H., G. Thompson, V. Tatarskii, 2009: Impact of Cloud Microphysics on the Development of Trailing Stratiform Precipitation in a Simulated Squall Line: Comparison of One– and Two–Moment Schemes. Mon. Wea. Rev., 137, 991–1007. doi:10.1175/2008MWR2556.1

Roberts, N. M., and H. W. Lean, 2008: Scale-selective verification of rainfall accumulations from high-resolution forecasts of convective events. *Mon. Wea. Rev.*, **136**, 78–97, doi:10.1175/2007MWR2123.1.

SOKOL, Z. Assimilation of extrapolated radar reflectivity into a NWP model and its impact on a precipitation forecast at high resolution. Atmospheric Research, v. 100, n. 2, p. 201-212, 2011.

SKAMAROCK, W.C.; KLEMP, J.B.; DUDHIA, J.; GILL, D.O.; BARKER, D.M.; DUDA, M.G.; HUANG, X.; WANG, W.; POWERS, J.G. A description of the advanced research WRF version 3. National Center for Atmospheric Research, 2008. 125 p. NCAR TECHNICAL NOTE.

Stensrud D.J., Louis J. Wicker, Ming Xue, Daniel T. Dawson, Nusrat Yussouf, Dustan M. Wheatley, Therese E. Thompson, Nathan A. Snook, Travis M. Smith, Alexander D. Schenkman, Corey K. Potvin, Edward R. Mansell, Ting Lei, Kristin M. Kuhlman, Youngsun Jung, Thomas A. Jones, Jidong Gao, Michael C. Coniglio, Harold E. Brooks, Keith A. Brewster, 2013: Progress and challenges with Warn-on-Forecast, Atmospheric Research,Volume 123, Pages 2-16,

Sun, J.-H., X.-L. Zhang, J. Wei, and S.-X. Zhao, 2005: A study on severe heavy rainfall in north China during the 1990s (in Chinese). Climatic Environ. Res, 10, 492–506.

Sun J, Xue M, Wilson JW, Zawadzki I, Ballard SP, Onvlee-Hooimeyer J, Joe P, Barker DM, Li PW, Golding B, Xu M, Pinto J. 2014. Use of NWP for nowcasting convective precipitation: Recent progress and challenges. Bull. Am. Meteorol. Soc. 95: 409–426, doi:10.1175/BAMS-D-11-00263.1.

Sun, J, H. Wang, W. Tong, Y. Zhang, C.-Y. Lin, and D. Xu, 2016: Comparison of the impacts of momentum control variables on high-resolution variational data assimilation and precipitation forecasting. Mon. Wea. Rev., 144, 149–169, doi:10.1175/MWR-D-14-00205.1.

Thompson, Gregory, Paul R. Field, Roy M. Rasmussen, William D. Hall, 2008: Explicit Forecasts of Winter Precipitation Using an Improved Bulk Microphysics

Scheme. Part II: Implementation of a New Snow Parameterization. Mon. Wea. Rev., 136, 5095–5115. doi:10.1175/2008MWR2387.1

Tong, W.; Li, G.; Sun, J.; Tang, X.; Zhang, Y. Design Strategies of an Hourly Update 3DVAR Data Assimilation System for Improved Convective Forecasting. Weather Forecast. 2016, 31, 1673–1695

Vendrasco, E. P., J. Sun, D. L. Herdies, and C. F. de Angelis, 2016: Constraining a 3DVAR Radar Data Assimilation System with Large-Scale Analysis to Improve Short-Range Precipitation Forecasts. *J. Appl. Meteor. Climatol.*, **55**, 673–690, https://doi.org/10.1175/JAMC-D-15-0010.1.

Wang, H., J. Sun, S. Y. Fan, and X. Y. Huang, 2013: Indirect assimilation of radar reflectivity with WRF 3D-VAR and its impact on prediction of four summertime convective events. J. Appl. Meteor. Climatol., 52, 889–902, doi:10.1175/ JAMC-D-12-0120.1.

Wu, D., X. Dong, B. Xi, Z. Feng, A. Kennedy, G. Mullendore, M. Gilmore, and W.-K. Tao (2013), Impacts of microphysical scheme on convective and stratiform characteristics in two high precipitation squall line events, J. Geophys. Res. Atmos., 118, 11,119–11,135, doi:10.1002/jgrd.50798.

Wolfensberger Daniel and Alexis Berne. From model to radar variables: a new forward polarimetric radar operator for COSMO. Atmos. Meas. Tech., 11, 3883–3916, 2018 https://doi.org/10.5194/amt-11-3883-2018.

Xiao, Q., Y. Kuo, J. Sun, W. Lee, D. M. Barker, and L. Eunha, 2007: An approach of radar reflectivity data assimilation and its assessment with the inland QPF of Typhoon Rusa (2002) at landfall. J. Appl. Meteor. Climatol., 46, 14–22, doi:10.1175/

JAM2439.1.

Zipser, E. Rainfall predictability: When will extrapolation-based algorithms fail? In Eighth Conference on Hydrometeorology, pages 138–142. American Meteorological Society, 1990.

List of tables

Table 1: Characteristics and data availability for each studied case.

Dates	Approximate time of severe weather reports	Convective mode	Available radar data
03 December 2016	1900 UTC	QLCS	SR, SL and CP
22 February 2017	1930 UTC	Isolated storm	SR, SL and CP
06 March 2017	1900 UTC	Storm cluster	SR and SL
05 May 2017	2100 UTC	QLCS	SR, SL and CP
27 October 2017	1900 UTC	Storm cluster	SR and CP

Table 2: Radars characteristics.

-	**São Roque (SR)**	**Salesópolis (SL)**	**Campinas (CP)**
Wavelength	10.9 cm (S-band)	10.638 cm (S-band)	3.202 cm (X-band)
Beamwidth	2.0°	0.968°	1.3°
Polarimetric	No	Yes	Yes
Doppler	Yes	Yes	Yes
Elevations	15	8	17
Radial resolution	500 m	250 m	200 m
Azimuthal resolution	1°	1°	1°

Table 3: Experiments

Experiment	Microphysics	With cycle	With DA
nCYnDA	Morrison/Thompson/WSM6/WDM6	No	No
nCYyDA	Morrison/Thompson/WSM6/WDM6	No	Yes
yCYnDA	Morrison/Thompson/WSM6/WDM6	Yes	No
yCYyDA	Morrison/Thompson/WSM6/WDM6	Yes	Yes

Table 4: Contingency table.

		Observed	
		Yes	*No*
Forecast	*Yes*	Hits	False alarms
	No	Misses	Correct negatives

List of figure captions:

FIG. 1: Map showing the location of the radars used in this study and the WRF domains. (a) Topography (m) from the d01 domain is shaded, and the WRF domains (d01, d02 and d03) are shown along with the radars location (colored dots) and coverage (colored circles). (b) Topography (m) from the d03 WRF domain is shaded, SR is the non-polarimetric S-band radar located in São Roque (red dot and circle with 250 km radius), SL is the polarimetric S-band radar of Salesópolis (orange dot and circle with 250 km radius), and CP represents the X-band polarimetric radar in Campinas (yellow dot and circle with 100 km radius).

FIG. 2: Composite reflectivity (dBZ) at (a) 1900 UTC 03 December 2016, (b) 1930 UTC 22 February 2017, (c) 1900 UTC 06 March 2017, (d) 2100 UTC 05 May 2017, and (e) 1900 UTC 27 October 2017. The reflectivity fields are generated by interpolating the reflectivity from the closest radar to the WRF d03 domain (Fig. 1). The arrows indicate the systems that caused severe weather, which occurred approximately in the times shown in the figures.

FIG. 3: Schematic diagram of the cycling strategy.

FIG. 4: GFS analysis of 500-hPa relative vertical vorticity (10^{-5} s^{-1}, shaded), geopotential height (dam, black contours every 3 dam), temperature (°C, grey dashed contours every 2°C), and winds (m s^{-1}, pennant is 25 m s^{-1}, full barb is 5 m s^{-1}, and half barb is 2.5 m s^{-1}) at 1800 UTC of (a) 03 December 2016, (b) 22 February 2017, (c) 06 March 2017, (d) 05 May 2017, (e) 27 October 2017. The d03 domain is shown in orange.

FIG. 5: Averaged vertical profiles of observation (OBS), innovation (OMB - observation minus background) and residual (OMA - observation minus analysis). The

average is performed over the entire grid where radar data are available and for all 5 cases.

FIG. 6: Increments (left), innovations (middle) and residuals (right) of snow (a) and graupel (b) at 10 km for the case of December 3rd, 2016. From the top are show the results for Morrinson, Thompson, WSM6 and WDM6.

FIG. 7: Temporal evolution of (a) RMSE and (b) FSS (using the 30-dBZ composite reflectivity as threshold) from 30 minutes forecasts (1830 UTC) to 3 hours forecasts (2100 UTC). Both RMSE and FSS are averages of all the five cases and the four assimilation methods.

FIG. 8: (a) Observed composite reflectivity at 2000 UTC 22 February 2017. Simulated composite reflectivity in domain d03 (1 km horizontal resolution) at 2000 UTC (2-h forecasts) 22 February 2017 of WRF runs (b) yCYyDA, Thompson, (c) yCYyDA, Thompson with reduced radius of influence of radar data (more details in the text), (d) yCYnDA, Thompson, (e) nCYyDA, Thompson, (f) nCYnDA, Thompson.

FIG. 9: (a,b,c) Observed composite reflectivity at 1900, 2000 and 2100 UTC 3 March 2017. Simulated composite reflectivity in domain d03 (1 km horizontal resolution) at 1900, 2000 and 2100 (1-, 2- and 3-h forecasts, respectively) 3 March 2017 of WRF runs (d,e,f) yCYyDA, (g,h,i) nCYyDA, (j,k,l) yCYnDA and (m,n,o) nCYnDA and Thompson microphysics scheme.

FIG. 10: (a) Average RMSE, (b) CSI, (c) POD and (d) FAR of all the 5 cases and simulations using all the four microphysics schemes for each DA method according to the line colors. Only values from 1830 UTC (30-minutes forecasts) to 2100 UTC (3-h forecasts) are shown.

List of figures:

FIGURE 1:

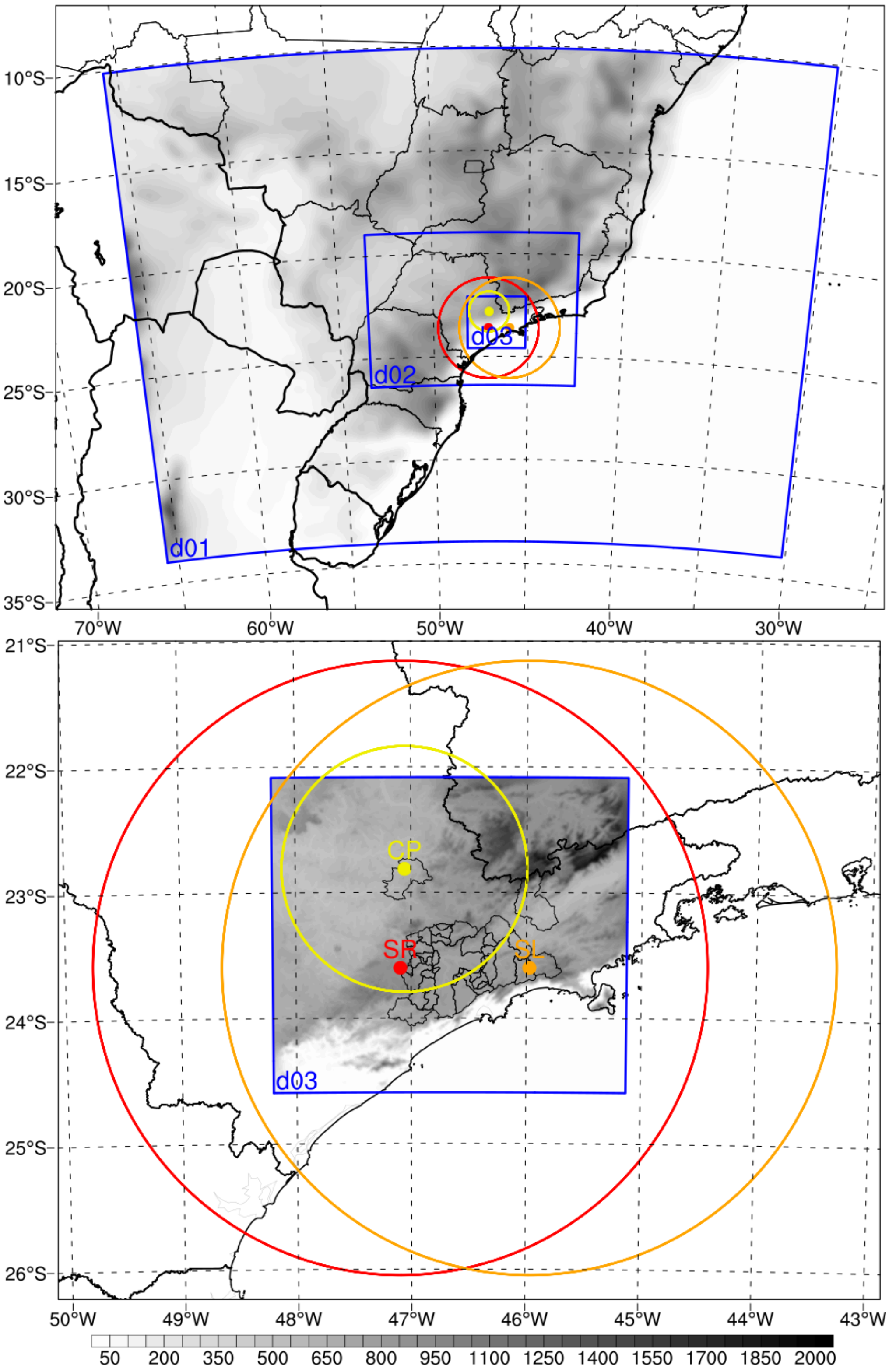

FIGURE 2:

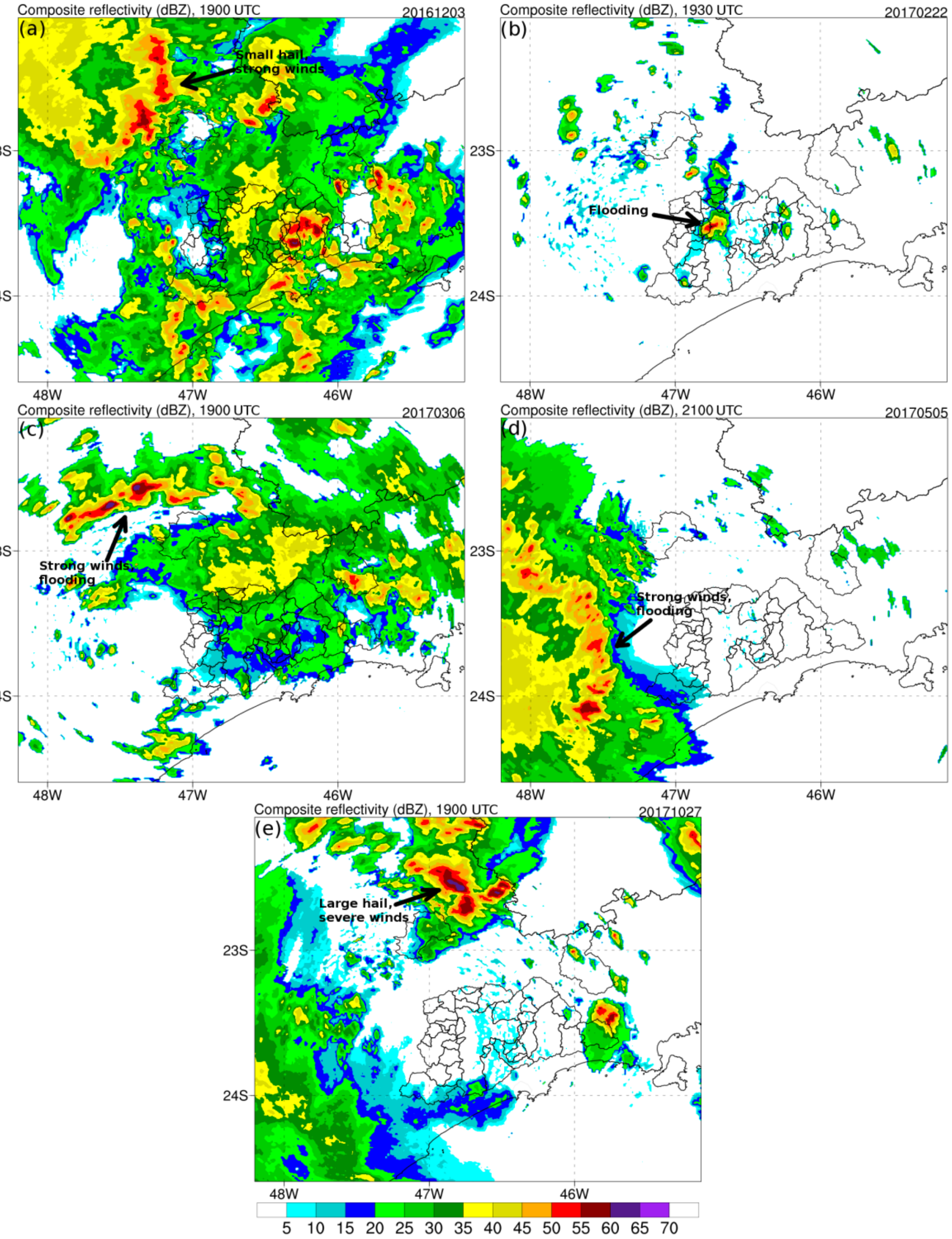
Composite reflectivity (dBZ), 1900 UTC
20161203
(a)
Small hail,
strong winds
Composite reflectivity (dBZ), 1930 UTC
20170222
(b)
Flooding
Composite reflectivity (dBZ), 1900 UTC
20170306
(c)
Strong winds,
flooding
Composite reflectivity (dBZ), 2100 UTC
20170505
(d)
Strong winds,
flooding
Composite reflectivity (dBZ), 1900 UTC
20171027
(e)
Large hail,
severe winds
23S
24S
48W
47W
46W
5 10 15 20 25 30 35 40 45 50 55 60 65 70

FIGURE 3:

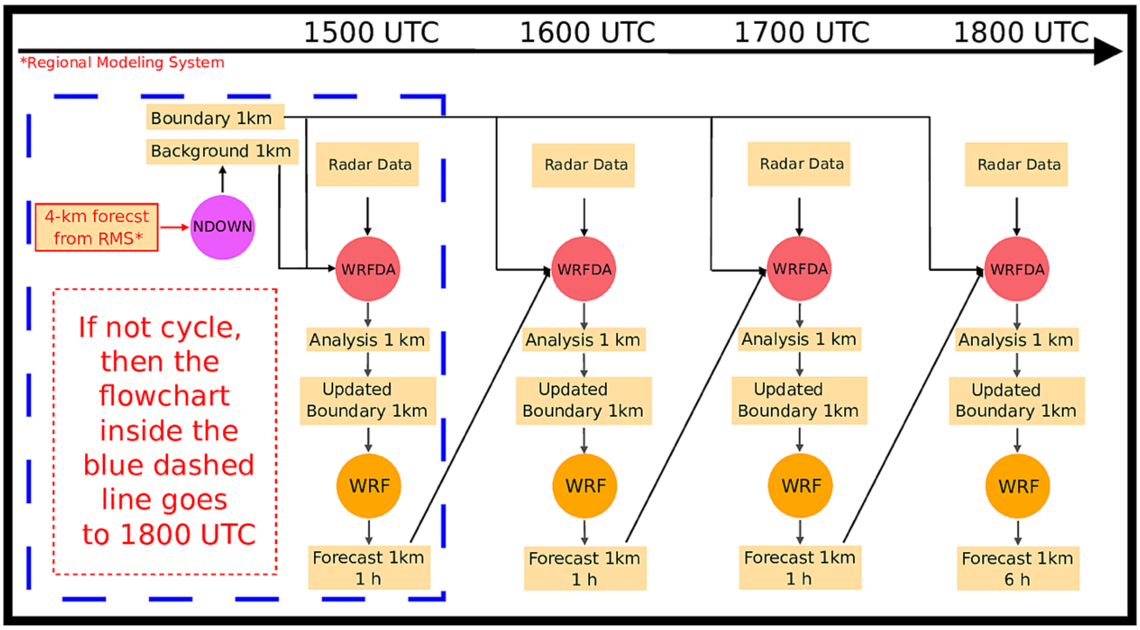

1500 UTC
1600 UTC
1700 UTC
1800 UTC
*Regional Modeling System
Boundary 1km
Background 1km
4-km forecst from RMS*
NDOWN
Radar Data
WRFDA
Analysis 1 km
Updated Boundary 1km
WRF
Forecast 1km 1 h
Forecast 1km 6 h
If not cycle, then the flowchart inside the blue dashed line goes to 1800 UTC

620 FIGURE 4:

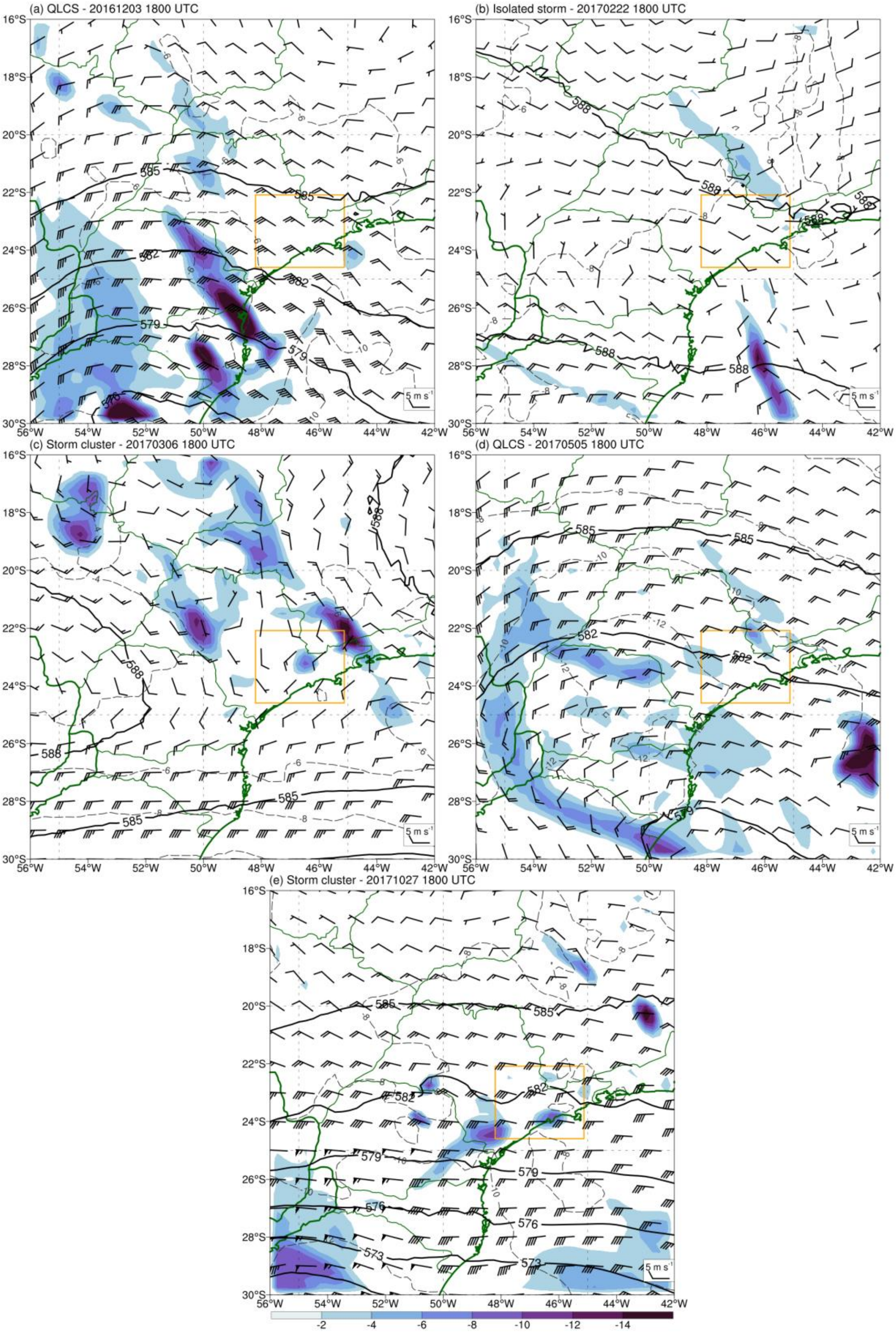

621

FIGURE 5:

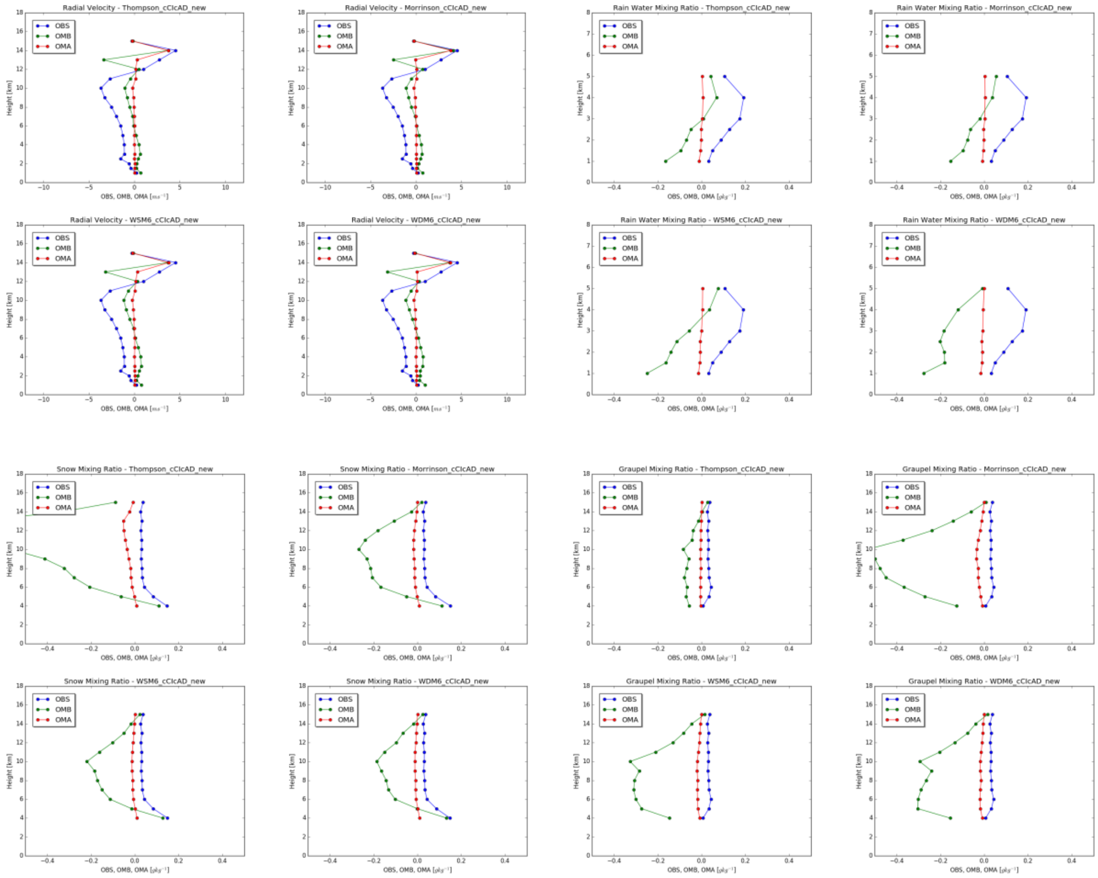
Radial Velocity - Thompson_cClcAD_new
Radial Velocity - Morrinson_cClcAD_new
Rain Water Mixing Ratio - Thompson_cClcAD_new
Rain Water Mixing Ratio - Morrinson_cClcAD_new
Radial Velocity - WSM6_cClcAD_new
Radial Velocity - WDM6_cClcAD_new
Rain Water Mixing Ratio - WSM6_cClcAD_new
Rain Water Mixing Ratio - WDM6_cClcAD_new
Snow Mixing Ratio - Thompson_cClcAD_new
Snow Mixing Ratio - Morrinson_cClcAD_new
Graupel Mixing Ratio - Thompson_cClcAD_new
Graupel Mixing Ratio - Morrinson_cClcAD_new
Snow Mixing Ratio - WSM6_cClcAD_new
Snow Mixing Ratio - WDM6_cClcAD_new
Graupel Mixing Ratio - WSM6_cClcAD_new
Graupel Mixing Ratio - WDM6_cClcAD_new
OBS
OMB
OMA
Height [km]
OBS, OMB, OMA

FIGURE 6:

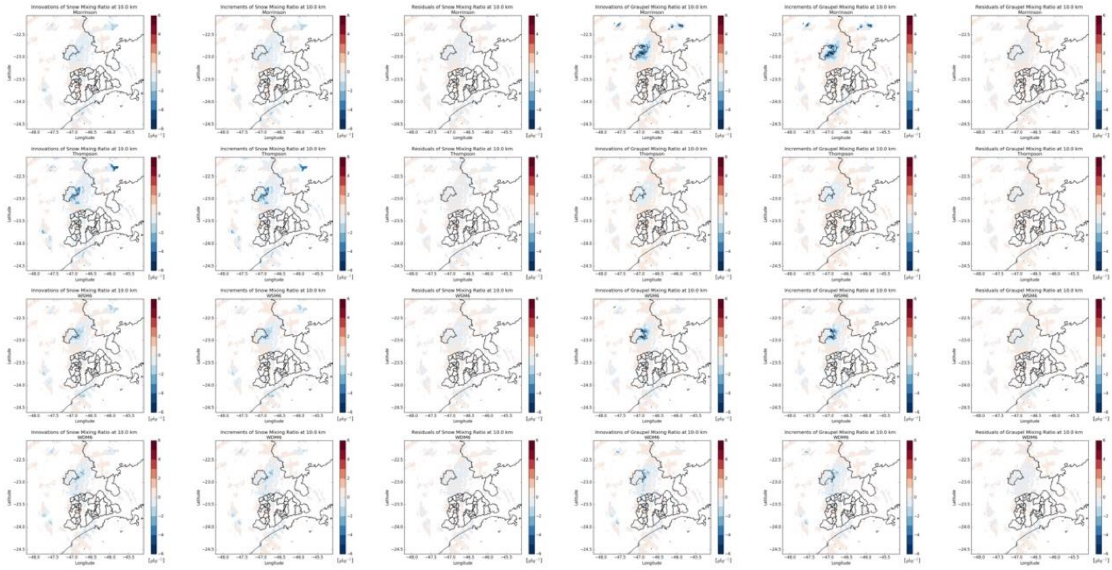

(a) (b)

FIGURE 7:

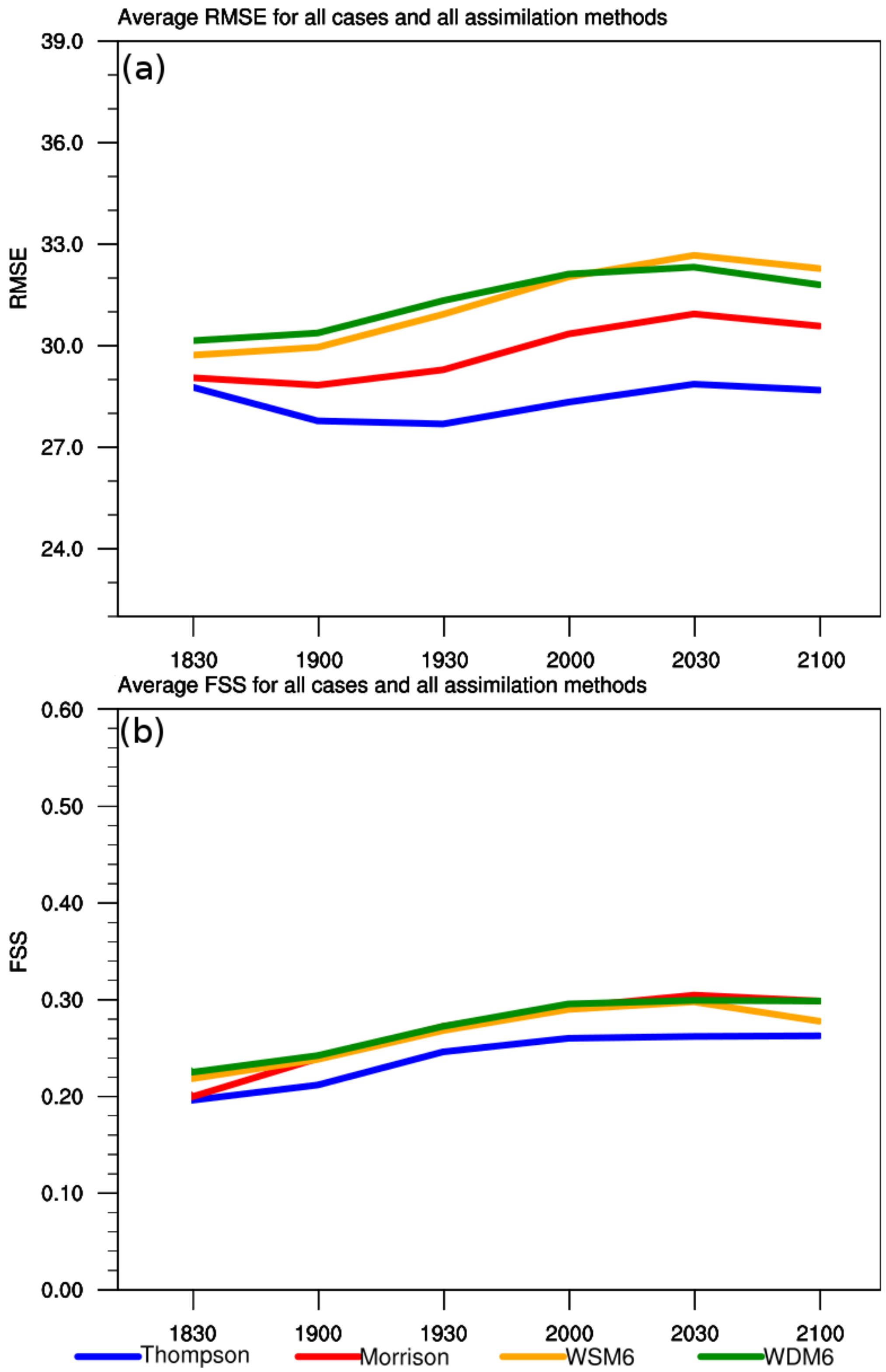
Average RMSE for all cases and all assimilation methods
(a)
RMSE
39.0
36.0
33.0
30.0
27.0
24.0
1830
1900
1930
2000
2030
2100
Average FSS for all cases and all assimilation methods
(b)
FSS
0.60
0.50
0.40
0.30
0.20
0.10
0.00
1830
1900
1930
2000
2030
2100
Thompson
Morrison
WSM6
WDM6

FIGURE 8:

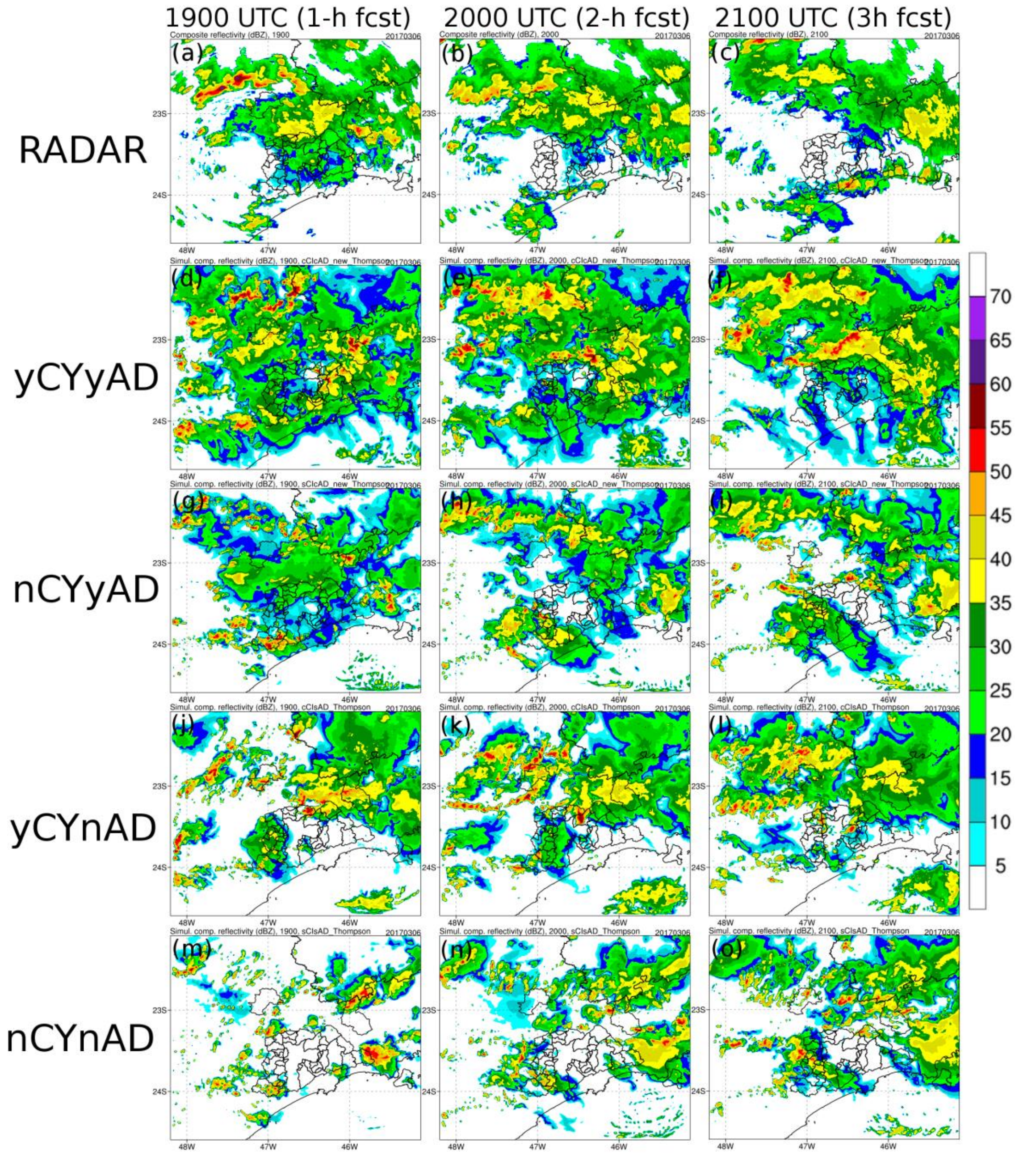
1900 UTC (1-h fcst)
2000 UTC (2-h fcst)
2100 UTC (3h fcst)
RADAR
yCYyAD
nCYyAD
yCYnAD
nCYnAD
(a)
(b)
(c)
(d)
(e)
(f)
(g)
(h)
(i)
(j)
(k)
(l)
(m)
(n)
(o)
70
65
60
55
50
45
40
35
30
25
20
15
10
5

FIGURE 9:

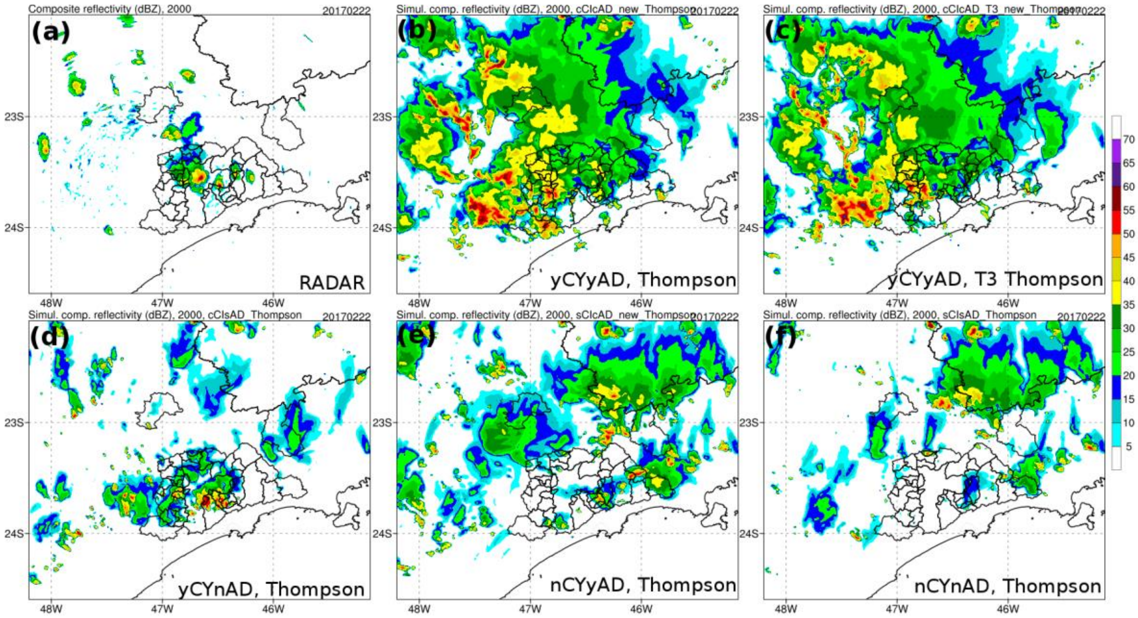
Composite reflectivity (dBZ), 2000
20170222
(a)
RADAR
Simul. comp. reflectivity (dBZ), 2000, cClcAD_new_Thompson
(b)
yCYyAD, Thompson
Simul. comp. reflectivity (dBZ), 2000, cClcAD_T3_new_Thompson
(c)
yCYyAD, T3 Thompson
Simul. comp. reflectivity (dBZ), 2000, cClsAD_Thompson
(d)
yCYnAD, Thompson
Simul. comp. reflectivity (dBZ), 2000, sClcAD_new_Thompson
(e)
nCYyAD, Thompson
Simul. comp. reflectivity (dBZ), 2000, sClsAD_Thompson
(f)
nCYnAD, Thompson
23S
24S
48W
47W
46W
70
65
60
55
50
45
40
35
30
25
20
15
10
5

FIGURE 10:

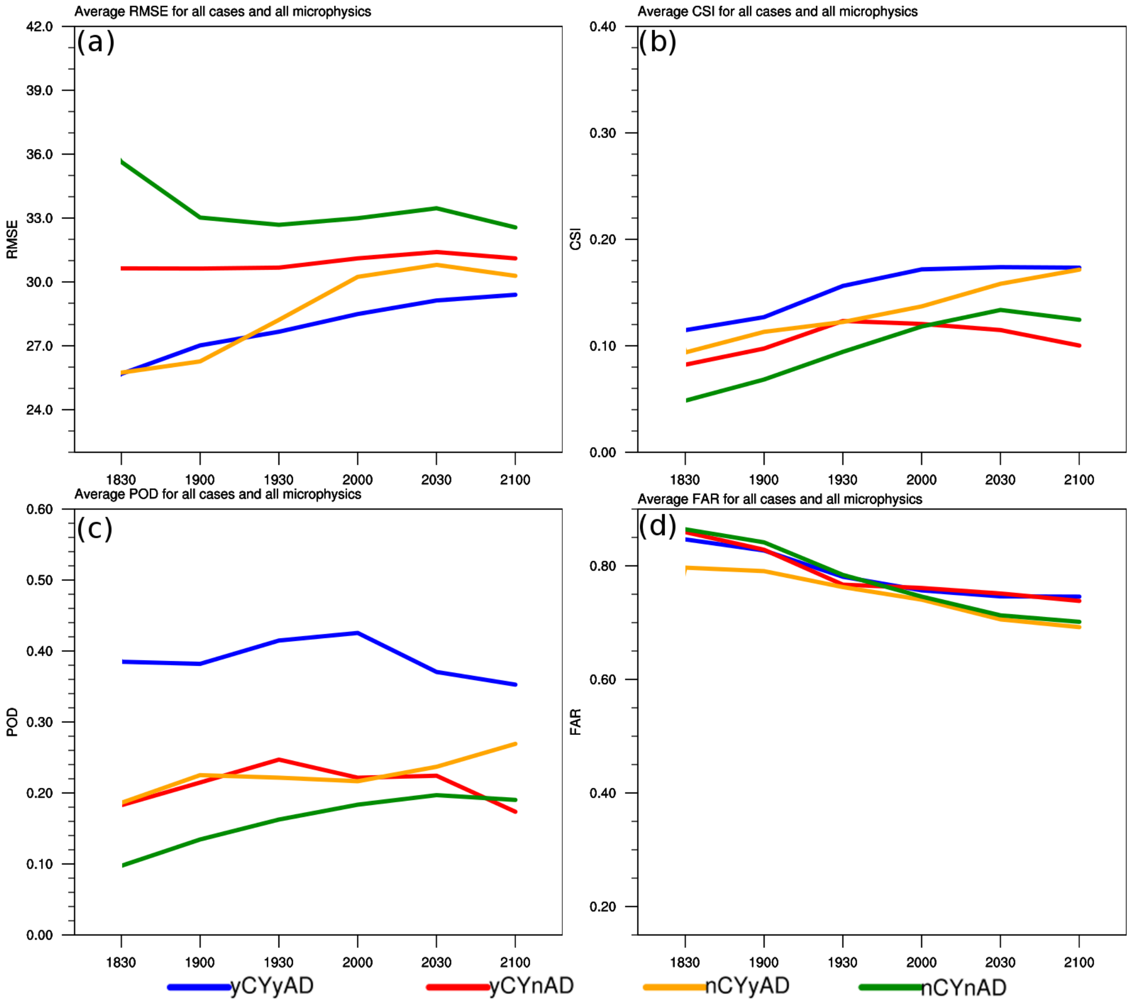
Average RMSE for all cases and all microphysics
(a)
RMSE
42.0
39.0
36.0
33.0
30.0
27.0
24.0
Average CSI for all cases and all microphysics
(b)
CSI
0.40
0.30
0.20
0.10
0.00
Average POD for all cases and all microphysics
(c)
POD
0.60
0.50
0.40
0.30
0.20
0.10
0.00
Average FAR for all cases and all microphysics
(d)
FAR
0.80
0.60
0.40
0.20
1830
1900
1930
2000
2030
2100
yCYyAD
yCYnAD
nCYyAD
nCYnAD